




Influence of La³⁺ substitution on the structural, magnetic and electrical characteristics of Sr₂FeTiO₆ double perovskites

J. Stella Punitha¹, A. Nataraj¹, V. Anbarasu², M. Dhilip³, M. Manikandan⁴, and K. Saravana Kumar^{5,*} 

¹Department of Physics, SRM Institute of Science & Technology, Ramapuram Campus, Chennai 600 089, Tamil Nadu, India

²Department of Physics (Unaided), PSG College of Arts & Science, Coimbatore, Tamil Nadu 641 014, India

³Microwave Tube Research Centre, Defence Research and Development Organisation, Bengaluru, Karnataka 560 013, India

⁴Department of Physics, National University of Singapore, 2 Science Drive 3, Singapore 117551, Republic of Singapore

⁵Department of Physics, Sri S. Ramasamy Naidu Memorial College, Sattur, Tamil Nadu 626 203, India

Received: 4 December 2022

Accepted: 7 June 2023

© The Author(s), under exclusive licence to Springer Science+Business Media, LLC, part of Springer Nature 2023

ABSTRACT

In this study, the La³⁺ ions are substituted at the Sr²⁺ site in Sr₂FeTiO₆ double perovskites using the solid state reaction method. The impact of La³⁺ ion substitution on the Sr₂FeTiO₆ physical characteristics have been studied. The SrTiO₃ structural parameters were utilised as starting model for performing the Rietveld refinement of powder X-ray diffraction patterns. Cubic symmetry with *Pm3m* space group was determined for the prepared materials. Due to the larger ionic radii of La³⁺ ion, the La substituted samples showed slight increase in the lattice cell parameters leading to volume expansion. The La-substituted samples don't exhibit any significant morphological differences when compared to parent compound. The diffused reflectance measurements also show no significant changes in the band gap values of La-substituted samples in comparison with the pure compound. The magnetization studies exhibit the enhanced ferromagnetic nature of La-substituted sample. Thermally activated charge carriers are also evident from the analysis of temperature dependent dielectric measurements.

1 Introduction

Exploring the double perovskite materials for their magnetic and electrical properties is mostly carried out by alkaline earth or lanthanide element substitution at the A-site and transition metals at the B site.

Due of the diverse variety of properties they exhibit, perovskite and double perovskite oxides with the general formulas ABO₃ and A₂BB'O₆ are of great interest. Double perovskites have attracted a lot of attention over the years due to their unique electrical and magnetic properties [1]. They are basically

Address correspondence to E-mail: kskumar23@hotmail.com

described by the equation $A_2BB'O_6$, where the A site is occupied by alkaline earth metals like Ba, Ca, Sr, and other similar ions, as well as rare earth ions with larger ionic radii [2]. The transition metal cations, alternatively, occupy the B octahedral positions, while lanthanides with smaller ionic radii do so for rare earth ions [3–6]. Double perovskites have an unusual combination of magnetic, dielectric, and conductivity properties depending on the degree of octahedral tilting [7, 8]. Interesting properties like magneto capacitance, multiferroicity [9, 10], magnetodielectric [11], ferroelectricity [12], spintronics for magnetic storage devices [13], thermopower [14] and thermoelectricity [15] towards technological applications have been shown by these perovskite and double perovskite materials.

Half metallic Sr_2FeMoO_6 , which displayed extremely high magneto-resistance at room temperature, was used to conduct the initial research on the magneto-resistance of strontium-based double perovskites [16–18]. The compound Sr_2FeMoO_6 was used to study the magneto-caloric effect because it exhibited ferromagnetic ordering and may be used for ferromagnetic refrigeration [19]. It was this substance that led to the discovery of the random anisotropy magnetic effect [20–22]. Low field colossal magneto resistance at room temperature is a feature of the compound Sr_2FeMoO_6 [23]. The compound Sr_2FeCoO_6 , which derives from the substitution of the Co-ion for Mo-ion, induces a spin glass state with mild ferromagnetic ordering [24]. A ferromagnetic to paramagnetic transition that happens when Mo-ions are swapped out for Mn-ions is investigated using dielectric measurements [25]. There has been very few research on strontium-based double perovskites with Ti ions at the B/B' site. Sr_2TiMnO_6 exhibited canted antiferromagnetic behaviour [26], Sr_2TiMoO_6 was utilised to research thermoelectric applications [27], and Sr_2FeTiO_6 compound showed spin glass behaviour [28]. Since transition metals are substituted for rare earth elements in the B site and alkaline earth elements in the A site, the current work examines how these modifications affect the magnetic and electrical properties.

The Sr_2FeTiO_6 [29] exhibited relaxor ferroelectric and magnetic spin glass properties that are interesting to observe [28]. This may be possible because the structure is a solid state mixture of $SrTiO_3$ and $SrFeO_3$. The Ti ion is known for its structural stability with its choice of crystallographic position. Similarly,

the Fe ions produce disorder in the structure. In the current work, Mo ion has been replaced with Ti ion while La ion has been substituted in the A site, producing the double perovskite $Sr_{2-x}La_xFeTiO_6$. The examination of the literature reveals that there have been no previous reports on the synthesis or characterisation of rare earth substituted Sr_2FeTiO_6 double perovskite compounds. In order to investigate $Sr_{2-x}La_xFeTiO_6$ compounds, the synthesis has been carried out using a conventional solid state reaction technique. The following discussion covers the experimental details and results.

2 Experimental

High purity powders of $SrCO_3$ (99% purity, Spectrum Veagents and Chemicals), La_2O_3 (99% purity, Alfa Aesar), TiO_2 (99% purity, Alfa Aesar), and Fe_2O_3 (99% purity, Alfa Aesar) are combined in stoichiometric ratios in atomic weight% and ground for nearly two hours in an agate mortar. The $Sr_{2-x}La_xFeTiO_6$ compounds ($x = 0, 0.2, 0.4, 0.6, \text{ and } 0.8$) have been synthesised using the solid state reaction method. In the beginning, the powdered powders were calcined at room temperature for 8 h at 1000 °C. The calcined materials were then reground for two hours and sintered at 1200 °C for eight hours. For a homogeneous mixture of substances, a similar approach has been used and the samples were sintered to 1200 °C for eight hours for another two times with intermediate grindings. Using a D8 Advance Bruker diffractometer, a powder x-ray diffraction analysis of the produced compounds was carried out at room temperature. To estimate the structural parameters, Rietveld refinement was performed using Full Prof software. Physical electronics (PH15000 Versa Probe III Scanning XPS Microprobe) device was used to conduct the x-ray photoelectron spectroscopy investigation in order to determine the oxidation states. Gaussian Lorentzian fitting with Shirley background is used to fit the spectrum obtained for La, Sr, Fe, Ti, and O using the CASA XPS software. For the examination of morphology, the Quanta 200 FEG FESEM apparatus was used to produce the field emission scanning electron micrographs. Utilizing a Perkin Elmer LAMBDA instrument, the diffused reflectance spectrum was obtained from a UV-Vis-NIR spectrophotometer. The Lakeshore VSM 7410 S equipment was used to conduct the

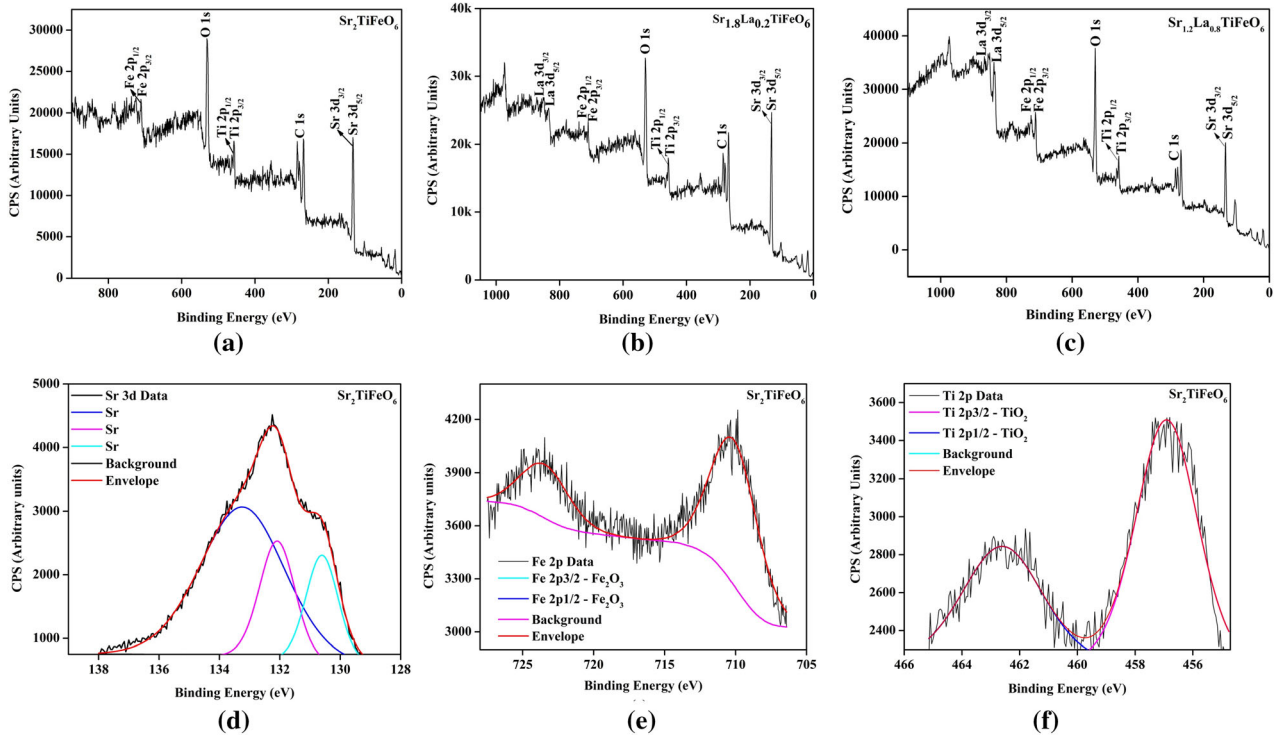


Fig. 1 a–c PS survey spectrum of the $\text{Sr}_{2-x}\text{La}_x\text{TiFeO}_6$ ($x = 0, 0.2, 0.8$) compounds. d–f Sr3d, Fe2p and Ti2p elemental spectrum of $\text{Sr}_2\text{TiFeO}_6$ compounds

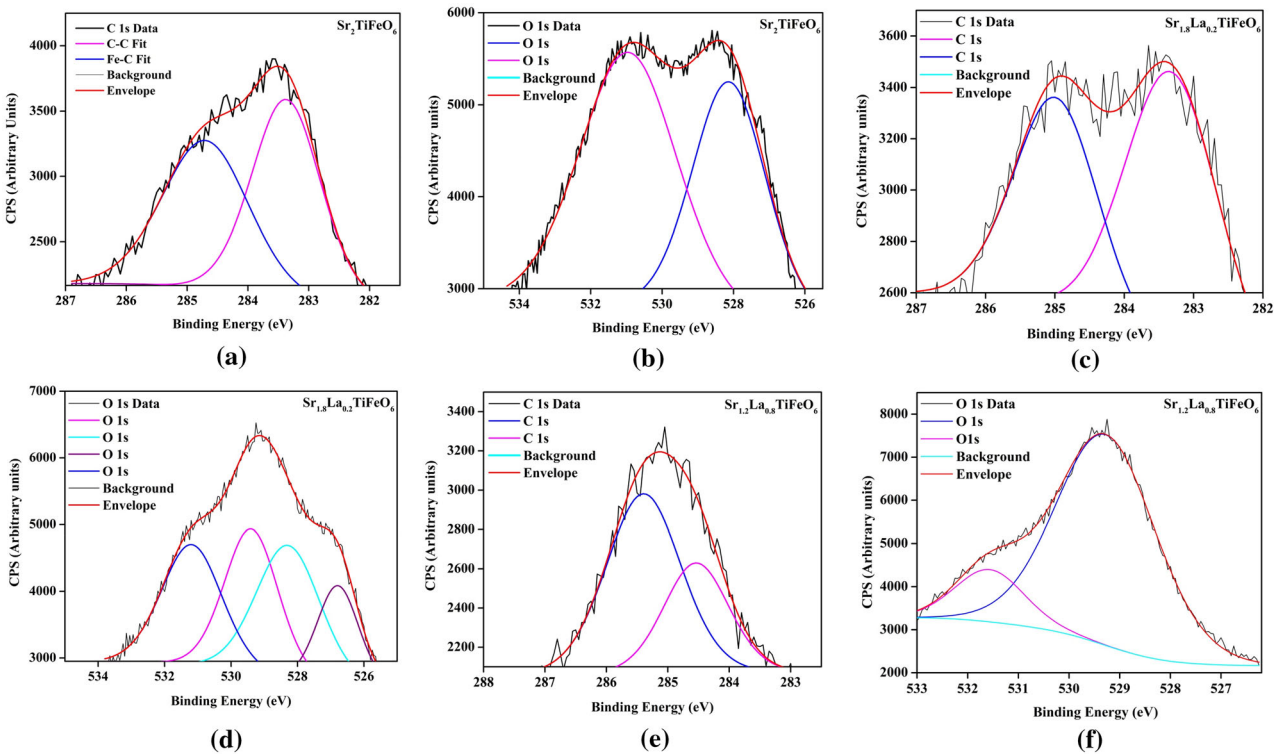


Fig. 2 a & b C1s and O1s spectrum of $\text{Sr}_2\text{TiFeO}_6$ compound. c & d C1s and O1s spectrum of $\text{Sr}_{1.8}\text{La}_{0.2}\text{TiFeO}_6$ compound. e & f C1s and O1s spectrum of $\text{Sr}_{1.2}\text{La}_{0.8}\text{TiFeO}_6$ compound

Table 1 Binding Energy values of C1s and O1s Spectrum

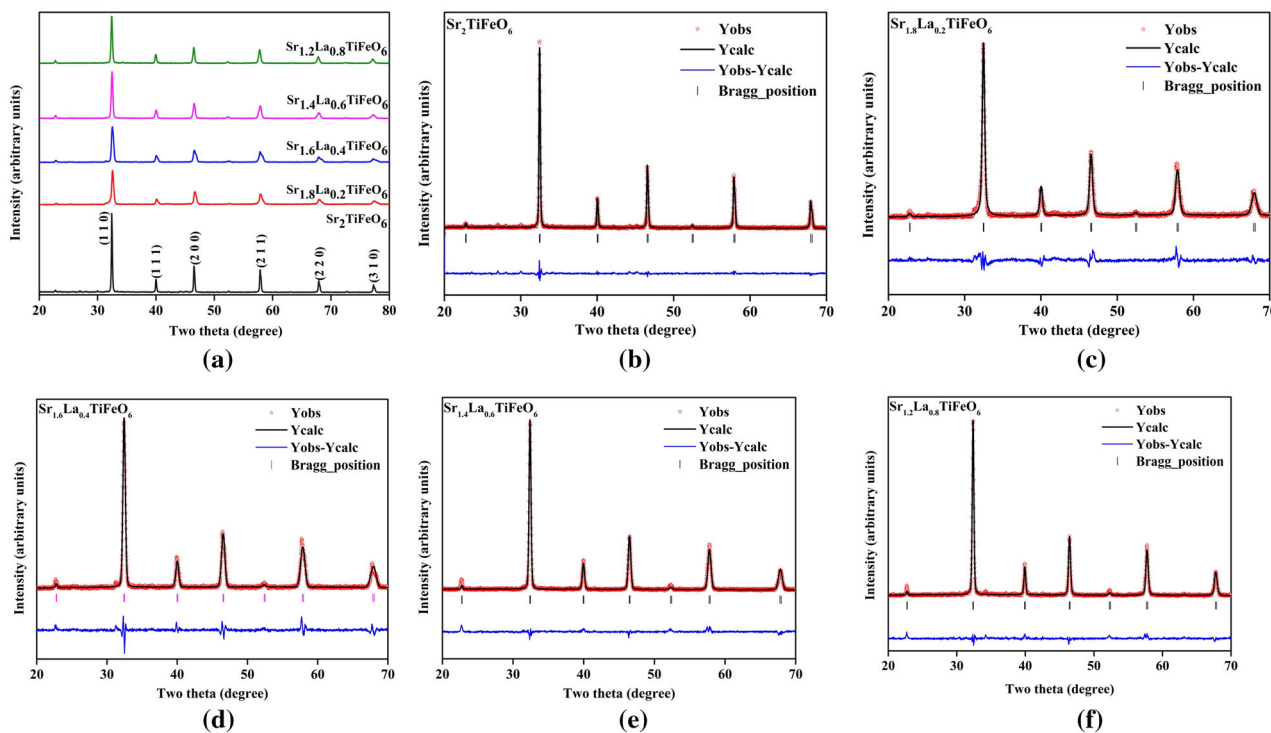
C 1s Fit	STFO	LSTFO1	LSTFO4	O 1s Fit	STFO	LSTFO1	LSTFO4
Fe–C	283.4	283.3	284.5	M–O	528.1	526.8	529.3
C–C	284.7	285	285.4	M–O	531.1	528.3	531.6
(284.8 eV)							
C–O–C (~ 286 eV)	–	–	–	M–O	–	529.4	–
O–C=O (288.5 eV)	–	–	–	C=O	–	531.2	–
				C–O	–	–	–

STFO = Sr₂TiFeO₆, LSTFO1 = La_{0.2}Sr_{1.8}TiFeO₆, LSTFO4 = La_{0.4}Sr_{1.6}TiFeO₆

Table 2 Binding Energy values of elements obtained from XPS spectrum

	Sr ₂ TiFeO ₆ (STFO) # (eV)	La _{0.2} Sr _{1.8} TiFeO ₆ (LSTFO1) # (eV)	La _{0.8} Sr _{1.2} TiFeO ₆ (LSTFO4) # (eV)
C 1s	284.7	285	284.5
O 1s	531.1	531.2	531.6
La 4d	–	836.7	838.1
Ti 2p	457	456.6	457.8
Fe 2p	710.4	710	710.5
Sr 2d	133.2	133.5	133.9

The values of Binding Energy as obtained from curve fitting of experimental data

**Fig. 3** a XRD patterns of the prepared samples. b–f X-ray Diffraction Rietveld refinement patterns of the Sr_{2-x}La_xTiFeO₆ (x = 0, 0.2, 0.4, 0.6, 0.8) compounds

magnetic measurements at room temperature. Dielectric readings at various frequencies and

temperatures were analysed using the Wagner Kerr LCR 4275 m device.

Table 3 The data obtained from Rietveld Refinement of XRD data is listed

	R _p	R _{wp}	R _{exp}	χ ²	a (Å)	b (Å)	c (Å)	Volume (Å ³)
Sr ₂ TiFeO ₆	4.42	5.76	4.83	1.44	3.8996	3.8996	3.8996	59.3029
Sr _{1.8} La _{0.2} TiFeO ₆	5.82	7.68	4.94	2.42	3.9009	3.9009	3.9009	59.3600
Sr _{1.6} La _{0.4} TiFeO ₆	5.60	7.24	5.09	2.03	3.9028	3.9028	3.9028	59.4457
Sr _{1.4} La _{0.6} TiFeO ₆	4.78	6.57	5.36	1.51	3.9077	3.9077	3.9077	59.6710
Sr _{1.2} La _{0.8} TiFeO ₆	5.00	6.71	5.41	1.54	3.9109	3.9109	3.9109	59.8169

Table 4 The structural parameters of Sr₂TiFeO₆

Atom	x	Y	z	Occupancy
Sr ₂ TiFeO ₆				
Sr1	0.5	0.5	0.5	1
Ti1	0	0	0	0.5
Fe1	0	0	0	0.5
O	0.5	0	0	3.0

Table 5 Important Bond angles and Bond lengths of Sr₂TiFeO₆

		Bond angles				
		Sr ₂ TiFeO ₆	Sr _{1.8} La _{0.2} TiFeO ₆	Sr _{1.6} La _{0.4} TiFeO ₆	Sr _{1.4} La _{0.6} TiFeO ₆	Sr _{1.2} La _{0.8} TiFeO ₆
Sr–O–Sr	90°	90°	90°	90°	90°	90°
Fe–O–Fe	180°	180°	180°	180°	180°	180°
Ti–O–Ti	180°	180°	180°	180°	180°	180°
Fe–O–Ti	180°	180°	180°	180°	180°	180°
Fe–O–Sr	90°	90°	90°	90°	90°	90°
Ti–O–Sr	90°	90°	90°	90°	90°	90°
		Bond Lengths				
		Sr ₂ TiFeO ₆ (Å)	Sr _{1.8} La _{0.2} TiFeO ₆ (Å)	Sr _{1.6} La _{0.4} TiFeO ₆ (Å)	Sr _{1.4} La _{0.6} TiFeO ₆ (Å)	Sr _{1.2} La _{0.8} TiFeO ₆ (Å)
Sr–O	2.7574	2.7584	2.7597	2.7532	2.7654	
Ti–O	1.9498	1.9505	1.9514	1.9539	1.9555	
Fe–O	1.9498	1.9505	1.9514	1.9539	1.9555	
	2.7574	2.7584	2.7597	2.7632	2.7654	

3 Results and discussion

3.1 X-Ray Photoelectron Spectroscopy Analysis (XPS)

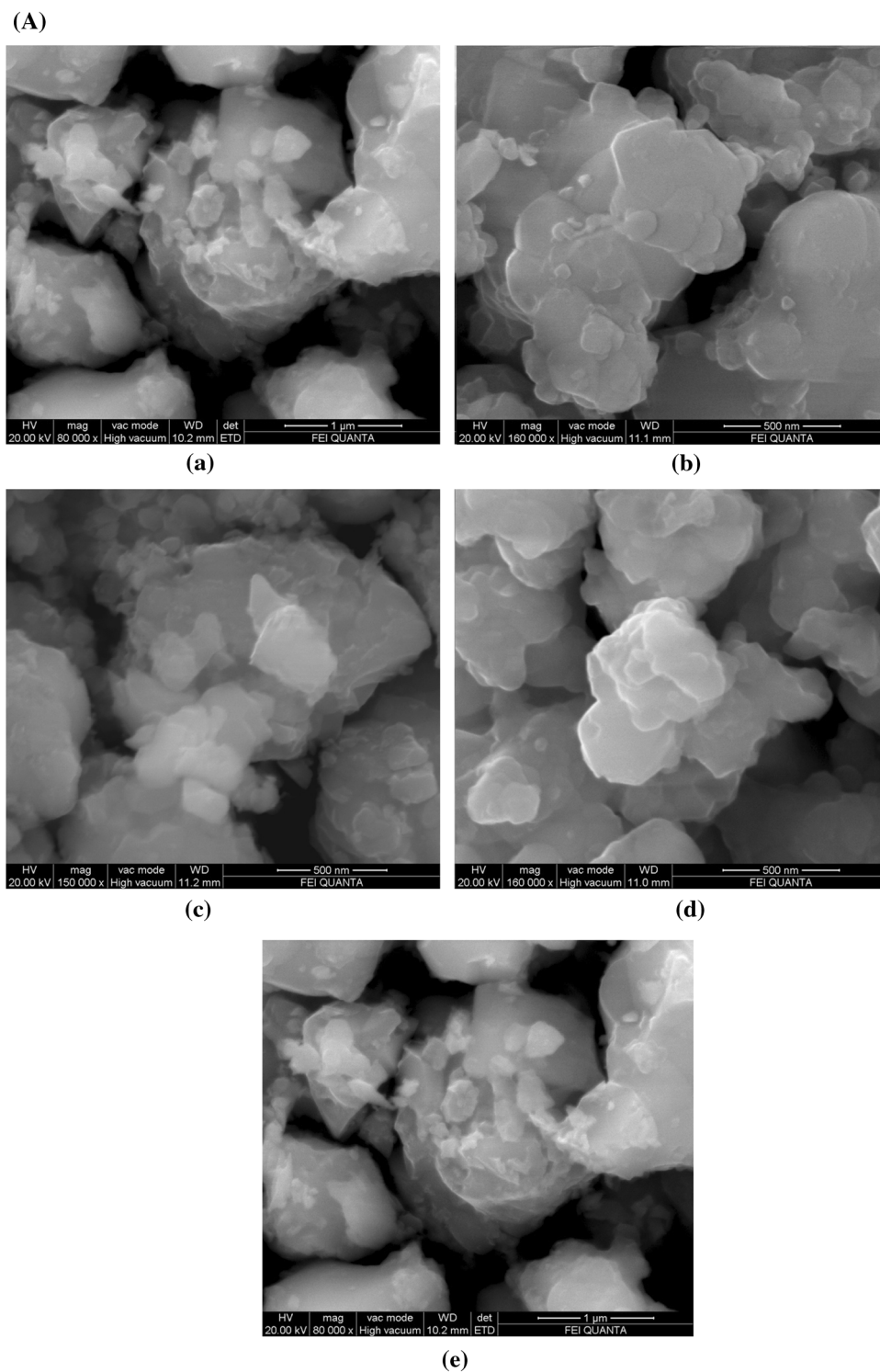
The oxidation states of the ions in the Sr₂TiFeO₆ (SFTO), Sr_{1.6}La_{0.2}TiFeO₆ (SLFTO1), and Sr_{1.2}La_{0.8}TiFeO₆ (SLFTO4) compounds were determined using XPS. The survey spectrum for the SFTO, SLFTO1, and SLFTO4 samples is shown in Fig. 1. All of the elements from the compound's stoichiometric

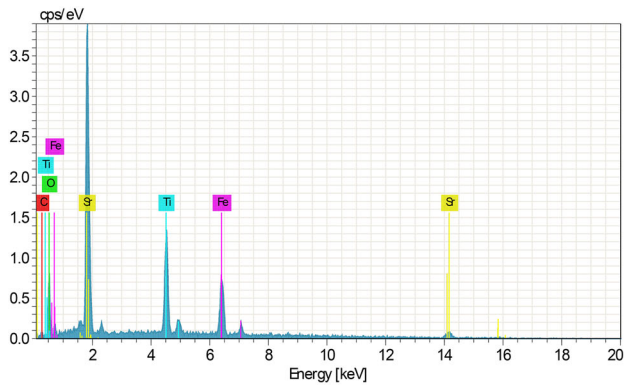
combination are present, according to the obtained survey spectrum of the samples. In the SFTO compound, the Fe ion is present in the + 3 oxidation state. This is evident by the fact that the binding energy value of the Fe-2p_{3/2} peak position determined by fitting at 710.7 eV closely resembles the binding energy value reported for the Fe₂O₃ molecule [30]. Additionally, it is observed that the Ti and Sr ions are present in + 4 and + 2 oxidation states, respectively, with reference to the binding energy values of TiO₂ and SrCO₃. The Fig. 2 displays the

carbon and oxygen peak fits for each prepared compound. The binding energy values determined using the fit obtained for elemental scans are displayed in the Tables 1 and 2. The binding energy values thus obtained for the SLFTO1 and SLFTO4 samples also

demonstrate the existence of Sr, Fe, and Ti in the + 2, +3, and + 4 oxidation states, respectively as well as La ion in the + 3 oxidation state. The XPS study therefore validates the incorporation of La ions into the double perovskite structure of $\text{Sr}_2\text{FeTiO}_6$.

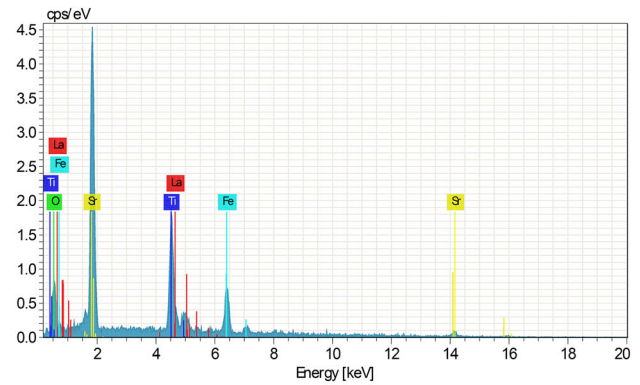
Fig. 4 **a** SEM micrographs of $\text{Sr}_{2-x}\text{La}_x\text{TiFeO}_6$ ($x = 0.0, 0.2, 0.4, 0.6, 0.8$) compounds. **b** EDX images of $\text{Sr}_{2-x}\text{La}_x\text{TiFeO}_6$ ($x = 0.0, 0.2, 0.4, 0.6, 0.8$) compounds





Test 2915

Element	At. No.	Mass [%]	Mass Norm. [%]	Atom [%]	abs. error [%] (1 sigma)	rel. error [%] (1 sigma)
Sr	38	44.06	46.13	18.60	1.96	4.45
O	8	21.78	22.80	50.35	5.26	24.15
Ti	22	12.98	13.59	10.03	0.47	3.66
Fe	26	12.56	13.15	8.32	0.48	3.81
C	6	4.12	4.32	12.70	2.28	55.34
		95.51	100.00	100.00		



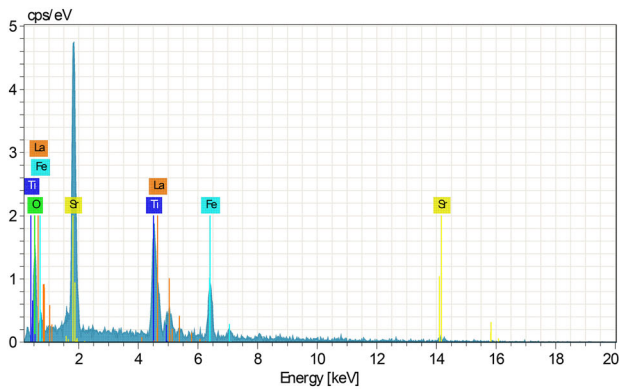
Test 1992

Element	At. No.	Mass [%]	Mass Norm. [%]	Atom [%]	abs. error [%] (1 sigma)	rel. error [%] (1 sigma)
Sr	38	46.37	43.26	19.01	2.07	4.46
O	8	26.95	25.14	60.52	6.20	23.01
Ti	22	15.78	14.72	11.84	0.57	3.59
Fe	26	10.24	9.55	6.59	0.42	4.14
La	57	7.84	7.32	2.03	0.36	4.57
		107.19	100.00	100.00		

(a)

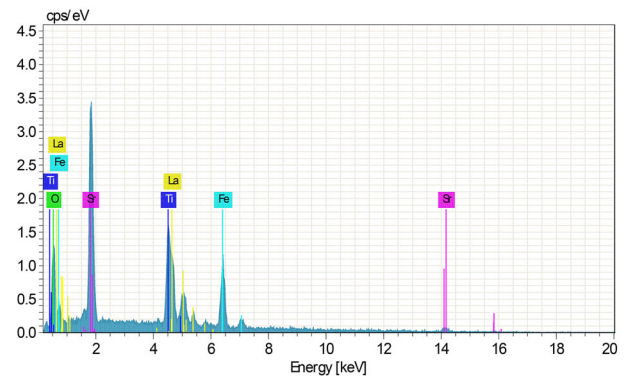
(b)

Fig. 4 continued



Test 1994

Element	At. No.	Mass [%]	Mass Norm. [%]	Atom [%]	abs. error [%] (1 sigma)	rel. error [%] (1 sigma)
Sr	38	40.45	35.22	14.62	1.89	4.66
O	8	33.49	29.17	66.31	7.83	23.38
La	57	16.03	13.96	3.66	0.66	4.14
Ti	22	13.89	12.09	9.19	0.56	4.05
Fe	26	10.97	9.55	6.22	0.51	4.65
		114.83	100.00	100.00		



Test 1993

Element	At. No.	Mass [%]	Mass Norm. [%]	Atom [%]	abs. error [%] (1 sigma)	rel. error [%] (1 sigma)
Sr	38	29.73	28.93	12.67	1.33	4.49
O	8	27.28	26.54	63.66	5.23	19.16
La	57	20.67	20.11	5.56	0.69	3.32
Fe	26	13.18	12.83	8.81	0.47	3.60
Ti	22	11.93	11.60	9.30	0.43	3.57
		102.79	100.00	100.00		

(c)

(d)

Fig. 4 continued

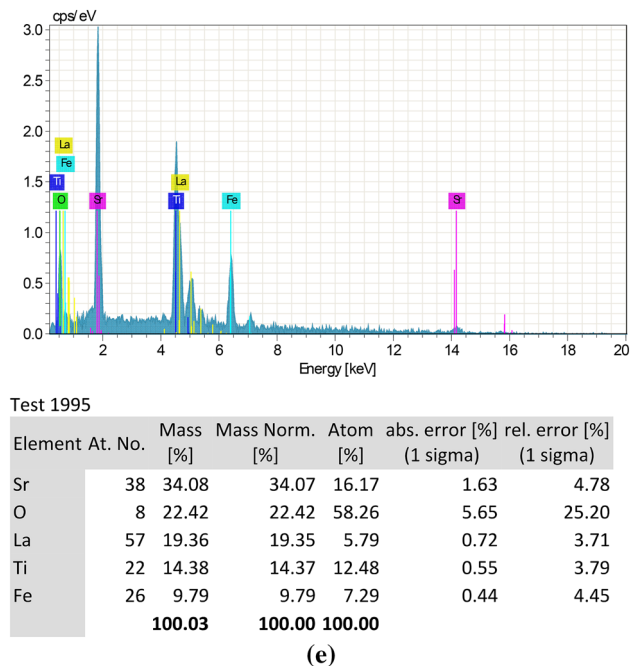


Fig. 4 continued

3.2 Powder X-ray diffraction (XRD) analysis

Figure 3a shows the $\text{Sr}_{2-x}\text{La}_x\text{FeTiO}_6$ ($x = 0, 0.2, 0.4, 0.6, 0.8$) samples powder x-ray diffraction patterns at room temperature. Using the FULLPROF Suite programme, the diffraction pattern was refined using the Rietveld method. The matching six-coefficient polynomial function is used to fit the background, while the pseudo-Voigt function is utilised to fit the peaks. As a starting point for the refinement, the SrTiO_3 structural parameters with cubic symmetry and $pm3m$ space group has been used. According to the results of Rietveld refinement, all of the La-substituted $\text{Sr}_2\text{FeTiO}_6$ compounds crystallize in single phase cubic symmetry system without any secondary phases. The dependability factors demonstrate a reasonable fit between the experimental and calculated patterns. The optimized XRD patterns are presented in the Fig. 3b–f, and the Tables 3 and 4 contains the calculated lattice parameters, reliability factors, bond angle, and bond distances. Significant bond lengths and bond angles are listed in Table 5.

3.3 SEM and EDS Analysis

Figure 4a shows the double perovskite SLTFO's surface microstructure. Because different-sized grains were present and evenly dispersed across the whole surface, the sample was likely prepared without voids. All samples exhibit the same morphologies and appear to be homogeneous and highly uniform. Due to the greater processing temperature, each sample has significant particle sizes and aggregates. The distribution, size, and form of the grains in the microstructure have revealed that the examined double perovskite samples are polycrystalline in nature. The micrographs also show the existence of small particles produced during preliminary grinding. Figure 4b shows the EDS patterns for the double perovskite SLTFO. The prepared sample's EDS spectra contained the elements Sr, Ti, Fe, La, and O, which ruled out the inclusion of any extraneous metals or elements. The element ratios utilised to prepared the samples are roughly matched by the atomic percentage values of each sample, as listed in Table 6.

3.4 Diffused Reflectance Spectroscopy (DRS) analysis

Figure 5a shows the diffuse reflectance UV–Vis spectra of $\text{Sr}_{2-x}\text{La}_x\text{TiFeO}_6$ ($x = 0.0, 0.2, 0.4, 0.6,$ and 0.8) that were taken in the range of 200 to 800 nm. Using the Kubelka–Munk function, the graph is plotted between $h\nu(1-R)^2/2R$ vs. $h\nu(\text{eV})$ as given in Fig. 5b. The intercepts are measured by extrapolating the sharp edges and by drawing a line along a sharp edge in order to determine the energy band gap value. Peak intensity rises with the La concentration in the compounds. The charge transfer transition between the doped La^{3+} and O^{2-} (valence and conduction band) in the lattice structure may have been brought on by a significant absorption. As the concentration of La^{3+} rises, the molecule’s reflectance value rises as well, which suggests that its absorbance properties are weakening. The absorption coefficient is derived using the Kubelka–Munk (KM) function using diffuse reflectance spectra, as illustrated in equation:

$$f(R) = \frac{\alpha}{s} = \frac{(1 - R)^2}{2R}$$

where $f(R)$ represents the KM function, α is the absorption coefficient, s is the scattering coefficient, and R is the reflection coefficient. The band gap values for the samples have been determined using the straight line fit in the graph shown in Fig. 5b. $\text{Sr}_{2-x}\text{La}_x\text{TiFeO}_6$ double perovskites have energy band gaps ranging from 2.0 to 2.6 eV for $x = 0.2, 0.4, 0.6,$ and 0.8 . The band gap values in the samples gradually increase as the La^{3+} doping concentration increases [31, 32].

3.5 Magnetization study

The vibrating sample magnetometer was used to analyse magnetization curves in order to evaluate the samples’ magnetic properties. Figure 6 displays the pure and La-substituted $\text{Sr}_2\text{TiFeO}_6$ samples’ field-dependent magnetization (M-H) curves. The Figure illustrates the narrowing of the hysteresis loops

Table 6 Values of atomic weight % obtained from EDS analysis of $\text{Sr}_{2-x}\text{La}_x\text{TiFeO}_6$ compounds and their Band Gap Values

Details of the compound	Weight %					Band gap value (eV)
	La	Sr	Ti	Fe	O	
$\text{Sr}_2\text{TiFeO}_6$	0	46.13	13.59	13.15	22.80	3.4
$\text{Sr}_{1.8}\text{La}_{0.2}\text{TiFeO}_6$	7.32	43.26	14.72	9.55	25.14	2.0
$\text{Sr}_{1.6}\text{La}_{0.4}\text{TiFeO}_6$	13.96	35.22	12.09	9.55	29.17	2.3
$\text{Sr}_{1.4}\text{La}_{0.6}\text{TiFeO}_6$	20.11	28.93	11.60	12.83	26.54	2.6
$\text{Sr}_{1.2}\text{La}_{0.8}\text{TiFeO}_6$	19.35	34.07	14.37	9.79	22.42	2.4

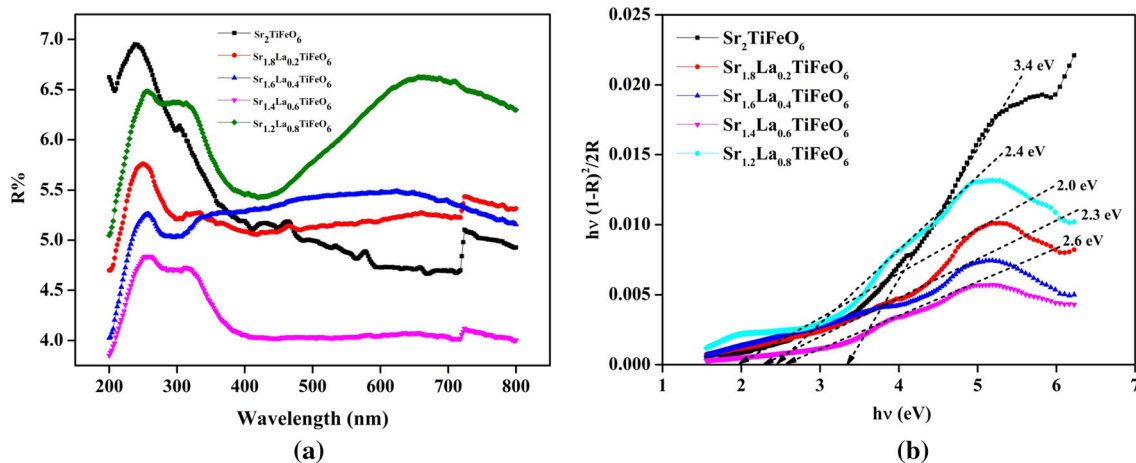


Fig. 5 **a** Diffused reflectance graph and **b** KM plot for the determination of energy band gap of $\text{Sr}_{2-x}\text{La}_x\text{TiFeO}_6$ ($x = 0.0, 0.2, 0.4, 0.6,$ and 0.8) compounds

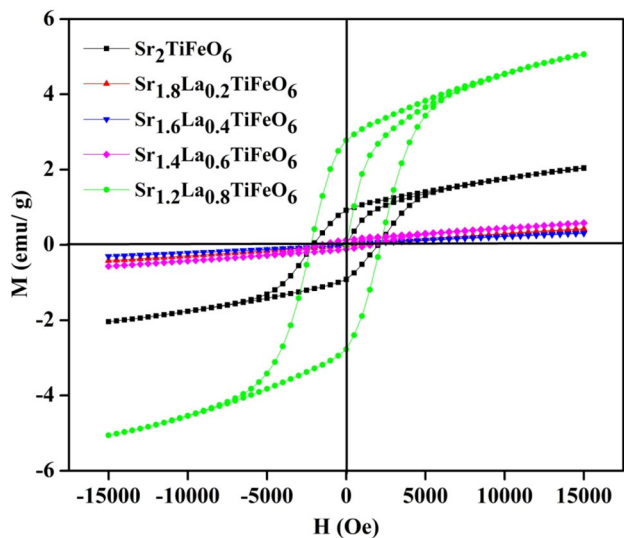


Fig. 6 Magnetization curves obtained for $Sr_{2-x}La_xTiFeO_6$ ($x = 0.0, 0.2, 0.4, 0.6$ and 0.8) compounds using VSM

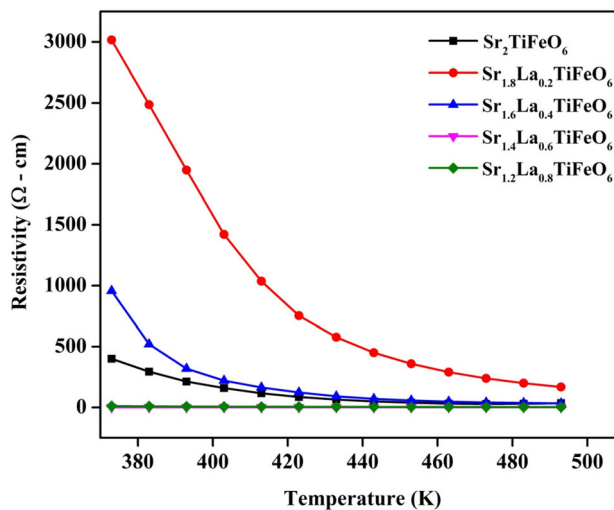


Fig. 8 Temperature dependent resistivity plots of $Sr_{2-x}La_xTiFeO_6$ ($x = 0.0, 0.2, 0.4, 0.6, 0.8$) compounds

Table 7 Magnetization properties of $Sr_{2-x}La_xTiFeO_6$ ($x = 0.0, 0.2, 0.4, 0.6, 0.8$) compounds

Compound details	Magnetic saturation (M_S) (emu/g)	Coercivity (H_c) Gauss	Magnetic retentivity (M_R) emu/g	Squareness ratio (M_R/M_S)
Sr_2TiFeO_6	24.542	2057.0	11.020	0.4490
$Sr_{1.8}La_{0.2}TiFeO_6$	6.0613	7.9661	4.9895	0.8231
$Sr_{1.6}La_{0.4}TiFeO_6$	5.2049	25.124	6.6069	1.2693
$Sr_{1.4}La_{0.6}TiFeO_6$	6.3589	1575.1	1.3397	0.2106
$Sr_{1.2}La_{0.8}TiFeO_6$	55.701	2198.6	30.548	0.5484

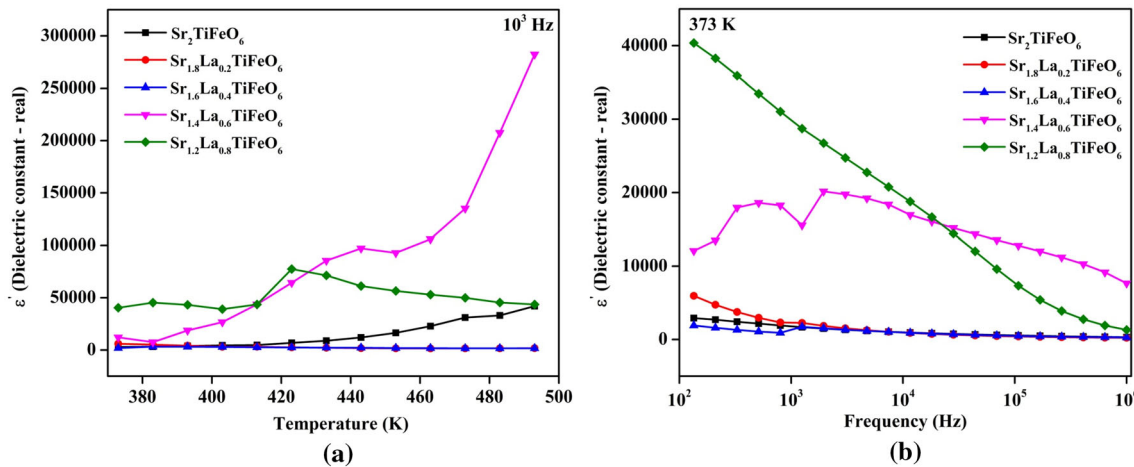


Fig. 7 **a** Temperature and **b** Frequency dependent dielectric constant plots of $Sr_{2-x}La_xTiFeO_6$ ($x = 0.0, 0.2, 0.4, 0.6, 0.8$) compounds

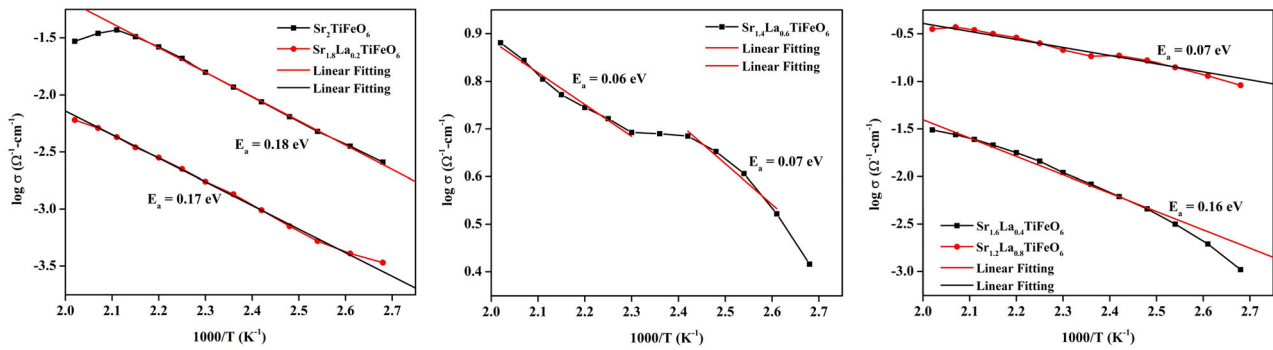


Fig. 9 Arrhenius plots for the determination of activation energy of $\text{Sr}_{2-x}\text{La}_x\text{TiFeO}_6$ ($x = 0.0, 0.2, 0.4, 0.6, 0.8$) compounds

with the La concentration. Saturation was attained at a maximum applied magnetic field of 15 KOe. There is a noticeable increase in the magnetization (saturation of magnetization, M_s) in this field with an increase in lanthanum. According to the magnetization value obtained at the maximum applied field, the $\text{Sr}_2\text{TiFeO}_6$ compound has ferromagnetic (FM) ordering. Due to the enhanced magnetization observed for the applied magnetic field, the highest magnetization values of the La^{3+} substituted samples show a substantial increase. Due to its high crystallinity and homogeneous morphologies as observed in SEM micrographs, the saturation magnetization (M_s) value for the $\text{Sr}_2\text{TiFeO}_6$ sample is relatively low when compared to La^{3+} ion replacement materials. This is a result of the formation of the magnetic perovskite structure as well, which happens when the most magnetic ions, as opposed to non-magnetic lanthanum ions, are substituted.

The coercivity (H_C) of the samples increases from 2057 G for pure to 2198 G for the sample with maximum La^{3+} replacement, as shown in the Table 7. Remanent magnetization (M_R) values (between 11.020 emu/g and 30.548 emu/g) rise parallel to the increase in La^{3+} ion concentration. The intrinsic and extrinsic features of the material affect coercivity and remanent magnetization.

The likelihood of substituent-induced structural disorder in the synthesised compounds is demonstrated by the gradual increase in coercive field and remanent magnetization, which also points to the integration of La^{3+} ions into the crystal lattice of the $\text{Sr}_2\text{TiFeO}_6$ combination. La^{3+} ions are thought to be present in the $\text{Sr}_2\text{TiFeO}_6$ structure, which is supported by the observed magnetization behaviour in the La^{3+} -substitution samples.

3.6 Dielectric analysis

Figure 7a illustrates the temperature dependent dielectric constant plot for various frequencies. The measured values of dielectric constant do not change, upto to about 415 K. However, after this temperature is reached, the observed values of dielectric constant start to rise. The frequency-dependent dielectric constant graph is shown in the Fig. 7b at various temperatures. For all substances, it is discovered that the dielectric constant value decreases with frequency. The variation of resistivity with temperature is shown in Fig. 8. The Arrhenius plot used to determine the activation energy (E_a) is shown in Fig. 9. Utilizing a straight-line equation and linear fitting, the activation energy is determined, and the results are displayed graphically. It is concluded from analysing the resistivity curves that the resistivity of the materials decreases with increase in temperature. This is due to the fact that thermally activated charge carriers are evident from the activation energy values of the samples (Fig. 9). This may happen due to the release of electrons and creation of more defects in the sample with increase in temperature which is generally observed in double perovskite materials.

4 Conclusion

Polycrystalline double perovskite $\text{Sr}_{2-x}\text{La}_x\text{FeTiO}_6$ ($x = 0, 0.2, 0.4, 0.6, 0.8$) samples were successfully synthesized having single phase nature using solid state reaction method. X-Ray photoelectron spectroscopy study proves that Sr, La, Fe, and Ti ions exist in + 2, +3, and + 4 oxidation states in the

double perovskite structure. The cubic $Pm\bar{3}m$ structure for the system with randomly arranged Fe and Ti cations at the octahedral sites were confirmed through the Rietveld refinement of X-ray diffraction data. With the substitution of lanthanide at the A-site of the double perovskite compound, the magnetic and conductivity properties were modified. The sample with highest La substitution showed a better ferromagnetic curve when compared to parent compound. The thermally activated charge carriers added to the conductivity of the prepared samples at high temperatures as revealed in temperature dependent dielectric studies.

Acknowledgements

The Authors thank and acknowledge Nanotechnology Research Centre (NRC), SRMIST for providing characterization facilities such as XPS, XRD UV-DRS and VSM.

Author contributions

JSP: Conceptualization of work, experimental work and discussion of data, creation of initial draft of the article, AN: Supervision of the work carried out for the article, discussion of obtained experimental data, VA: Discussion of obtained experimental data, MD: Discussion of obtained experimental data, MM: Discussion of obtained experimental data, KSK: Supervision of the work carried out for the article, discussion of obtained experimental data, finalization of article.

Funding

No funding was received to assist with the preparation of this manuscript.

Data availability

All data generated or analysed during this study are included in this published article.

Declarations

Conflict of interest The authors have no competing interests to declare that are relevant to the content of this article.

References

1. X. Ye, J. Zhao, H. Das et al., Observation of novel charge ordering and spin reorientation in perovskite oxide $PbFeO_3$. *Nat. Commun.* (2021). <https://doi.org/10.1038/s41467-021-22064-9>
2. Sami Vasala, Maarit Karppinen, $A_2B'B''O_6$ perovskites: A review (Elsevier, Amsterdam, 2015)
3. M.M. Arman, N.G. Imam, R. Loreda Portales, S.I. El-Dek, Synchrotron radiation X-ray absorption fine structure and magnetization improvement of A-site Ce^{3+} doped $LaFeO_3$. *J. Magn. Magn. Mater.* **513**, 167097 (2020). <https://doi.org/10.1016/J.JMMM.2020.167097>
4. N.G. Imam, G. Aquilanti, A.A. Azab, S.E. Ali, Correlation between structural asymmetry and magnetization in bi-doped $LaFeO_3$ perovskite: a combined XRD and synchrotron radiation XAS study. *J. Mater. Sci.* **32**, 3361–3376 (2021). <https://doi.org/10.1007/S10854-020-05084-X/METRICS>
5. T. Maiti, M. Saxena, P. Roy, Double perovskite ($Sr_2B'B''O_6$) oxides for high-temperature thermoelectric power generation—A review. *J. Mater. Res.* **34**, 107–125 (2019)
6. D. Kumar, R.S. Yadav, Monika, et al., Synthesis techniques and applications of Perovskite materials. *Perovskite Mater. Devices Integr.* (2020). <https://doi.org/10.5772/INTECHOPEN.86794>
7. K. Leng, Q. Tang, Y. Wei et al., Recent advances in re-based double perovskites: synthesis, structural characterization, physical properties, advanced applications, and theoretical studies. *AIP Adv.* (2020). <https://doi.org/10.1063/5.0031196>
8. S.M. Borchani, W.C.R. Koubaa, M. Megdiche, Structural, magnetic and electrical properties of a new double-perovskite $LaNaMnMoO_6$ material. *R. Soc. Open. Sci.* (2017). <https://doi.org/10.1098/rsos.170920>
9. N.A. Spaldin, Multiferroics: past, present, and future. *Phys. Today.* (2017). <https://doi.org/10.1557/mrs.2017.86>
10. M.P. Singh, K.D. Truong, S. Jandl, P. Fournier, Long-range Ni/Mn structural order in epitaxial double perovskite La_2NiMnO_6 thin films. *Phys. Rev. B.* (2009). <https://doi.org/10.1103/PhysRevB.79.224421>
11. R. Ranjith, A.K. Kundu, M. Filippi et al., Ferromagnetism and magnetodielectric effect in insulating $LaBiMn_{4/3}Co_2O_6$ thin films ferromagnetism and magnetodielectric effect in

- insulating LaBiMn_{4/3}Co_{2/3}O₆. *Appl. Phys. Lett.* **10**(1063/1), 2842409 (2012)
12. S.W. Cheong, M. Mostovoy, Multiferroics: a magnetic twist for ferroelectricity. *Nat. Mater.* **6**(1), 13–20 (2007). <https://doi.org/10.1038/nmat1804>
 13. B. Merabet, O.M. Ozkendir, A.S. Hassanien, M.A. Maleque, Spin-orbit coupling effect on the electronic structure of Sr₂FeHfO₆ alloy for spintronics application. *J. Magn. Magn. Mater.* **518**, 167374 (2021). <https://doi.org/10.1016/J.JMMM.2020.167374>
 14. P. Roy, T. Maiti, Colossal change in thermopower with temperature-driven p-n-type conduction switching in LaxSr_{2-x}TiFeO₆ double perovskites. *J. Phys. D.* (2018). <https://doi.org/10.1088/1361-6463/aaa284>
 15. D. Sri Gyan, V. Sundram, A. Dwivedi et al., Effect of B-site cation ordering on high temperature thermoelectric behavior of BaxSr_{2-x}TiFeO₆ double perovskites. *J. Phys. Condens. Matter.* (2020). <https://doi.org/10.1088/1361-648X/ab7575>
 16. H.F. Zhao, L.P. Cao, Y.J. Song et al., Structure, magnetic and electrical properties of disordered double perovskite Pb₂CrMoO₆. *Solid State Commun.* **204**, 1–4 (2015). <https://doi.org/10.1016/j.ssc.2014.12.001>
 17. F. Zhang, S. Li, J. Song et al., Magnetic characterization and low-temperature heat transport properties of the orthoferrites. *IEEE Trans. Magn.* **51**, 2–5 (2015). <https://doi.org/10.1109/TMAG.2015.2445916>
 18. X.-M. Feng, G.-Y. Liu, Q.-Z. Huang, G.-H. Rao, Influence of annealing treatment on structural and magnetic properties of double perovskite Sr₂FeMoO₆. *Trans. Nonferrous Metals Soc. China* (2006). [https://doi.org/10.1016/S1003-6326\(06\)0021-6](https://doi.org/10.1016/S1003-6326(06)0021-6)
 19. A.S. Erchidi Elyacoubi, R. Masrour, A. Jabar et al., Magnetic properties and magnetocaloric effect in double Sr₂FeMoO₆ perovskites. *Mater. Res. Bull.* **99**, 132–135 (2018). <https://doi.org/10.1016/j.materresbull.2017.10.037>
 20. J. Navarro, J. Nogués, J.S. Muñoz, J. Fontcuberta, Antisites and electron-doping effects on the magnetic transition of Sr₂FeMoO₆ double perovskite. *Phys. Rev. B* (2003). <https://doi.org/10.1103/PhysRevB.67.174416>
 21. D. Yang, R.J. Harrison, J.A. Schiemer et al., Magnetostructural coupling behavior at the ferromagnetic transition in double-perovskite Sr₂FeMoO₆. *Phys. Rev. B* (2016). <https://doi.org/10.1103/PhysRevB.93.024101>
 22. D. Sánchez, J.A. Alonso, M. García-Hernández et al., Origin of neutron magnetic scattering in antisite-disordered Sr₂FeMoO₆ double perovskites. *Phys. Rev. B* **65**, 1044261–1044268 (2002). <https://doi.org/10.1103/PhysRevB.65.104426>
 23. K.I. Kobayashi, T. Kimura, H. Sawada et al., Room-temperature magnetoresistance in an oxide material with an ordered double-perovskite structure. *Nature.* **395**, 677–680 (1998). <https://doi.org/10.1038/27167>
 24. R. Pradheesh, H.S. Nair, C.M.N. Kumar et al., Observation of spin glass state in weakly ferromagnetic Sr₂FeCoO₆ double perovskite. *J. Appl. Phys.* (2012). <https://doi.org/10.1063/1.3686137>
 25. D. Triyono, A. Hannisa, H. Laysandra, Structural, magnetic, and dielectric studies of cubically ordered Sr₂FeMnO₆. *Appl. Phys. A* (2022). <https://doi.org/10.1007/s00339-022-05372-9>
 26. K.R.S.P. Meher, M. Savinov, S. Kamba et al., Structure, dielectric, and magnetic properties of Sr₂TiMnO₆ ceramics. *J. Appl. Phys.* (2010). <https://doi.org/10.1063/1.3500369>
 27. M. Saxena, K. Tanwar, T. Maiti, Environmental friendly Sr₂TiMoO₆ double perovskite for high temperature thermoelectric applications. *Scr. Mater.* **130**, 205–209 (2017). <https://doi.org/10.1016/j.scriptamat.2016.11.033>
 28. P. Neenu Lekshmi, S. Savitha Pillai, K.G. Suresh et al., Room temperature relaxor ferroelectricity and spin glass behavior in Sr₂FeTiO₆ double perovskite. *J. Alloys Compd.* **522**, 90–95 (2012). <https://doi.org/10.1016/j.jallcom.2012.01.091>
 29. J.S. Punitha, M. Dhilip, V. Anbarasu et al., Coexistence of two phases in Sr₂TiFeO₆ double perovskite. *AIP Conf. Proc.* (2019). <https://doi.org/10.1063/1.5114590/748044>
 30. F.J. MOULDER, (1995) Handbook of X-Ray Photoelectron Spectroscopy. Physical Electronics division. pp 230–232
 31. M. Saleem, S. Tiwari, M. Soni et al., Structural, optical and other spectral studies of transition metal Ti⁴⁺-doped Zn-Cd oxide nanomaterials. *Int. J. Mod. Phys. B* (2020). <https://doi.org/10.1142/S0217979220500332>
 32. S. Aarif Ul Islam, M. Ikram, Structural stability improvement, Williamson Hall analysis and band-gap tailoring through A-site Sr doping in rare earth based double perovskite La₂NiMnO₆. *Rare Met.* **38**, 805–813 (2019). <https://doi.org/10.1007/s12598-019-01207-4>

Publisher's Note Springer Nature remains neutral with regard to jurisdictional claims in published maps and institutional affiliations.

Springer Nature or its licensor (e.g. a society or other partner) holds exclusive rights to this article under a publishing agreement with the author(s) or other rightsholder(s); author self-archiving of the accepted manuscript version of this article is solely governed by the terms of such publishing agreement and applicable law.